Journal of
Synchrotron Radiation

ISSN 0909-0495

Received 29 November 2012
Accepted 23 January 2013

Optimization of analyzer-based imaging systems for minimal surface absorbed dose

Brian E. Bewer

Experimental Facilities Division, Canadian Light Source, 44 Innovation Boulevard, Saskatoon, Saskatchewan, Canada S7N 2V3. E-mail: brian.bewer@lightsource.ca

Analyzer-based imaging has improved tissue X-ray imaging beyond what conventional radiography was able to achieve. The extent of the improvement is dependent on the crystal reflection used in the monochromator and analyzer combination, the imaging photon energy, the geometry of the sample and the imaging detector. These many factors determine the ability of the system to distinguish between various bone tissues or soft tissues with a specified statistical certainty between pixels in a counting detector before any image processing. The following discussion will detail changes in the required number of imaging photons and the resulting surface absorbed dose when the imaging variables are altered. The process whereby the optimal imaging parameters to deliver the minimum surface absorbed dose to a sample while obtaining a desired statistical certainty between sample materials for an arbitrary analyzer-based imaging system will be described. Two-component samples consisting of bone and soft tissue are discussed as an imaging test case. The two-component approach will then be generalized for a multiple-component sample.

Keywords: analyzer-based imaging; diffraction enhanced imaging; multiple image radiography.

1. Introduction

The analyzer-based imaging (ABI) method was pioneered by diffraction enhanced imaging (DEI) (Chapman *et al.*, 1997) and was later expanded to include multiple image radiography (MIR) where three or more images are required and ultra-small-angle scattering information about the sample becomes available (Rigon *et al.*, 2007). The additional sensitivity to density changes provided by the ABI method has enabled soft tissue imaging that would not be possible or would be dose prohibitive with conventional absorption imaging. The level of soft tissue contrast enhancement and dose reduction when measuring with the ABI method depends on the crystal refection used, the average refraction angle deviation of the incident X-rays, the imaging photon energy, and the imaging detector properties. Studies on human breast tissue using ABI have indicated a 15-fold reduction in X-ray dose when imaging at 30 keV while still obtaining a comparable or superior image than achievable with conventional absorption radiography at 18 keV (Pisano *et al.*, 2000; Keyriläinen *et al.*, 2005). In addition to soft tissues, recent studies examining bone tissues with the ABI method have enabled the visualization of micro-architecture that is not discernible in dual-energy X-ray absorptiometry (DEXA) imaging and may lead to more accurate estimates of bone density and bone strength in osteoporotic patients while delivering less dose than DEXA systems (Cooper *et al.*, 2011*a*,*b*). The following discussion describes how to optimize an ABI system for imaging biological tissues and minimize the surface absorbed dose delivered to patients or samples.

1.1. Refraction of X-rays

In the diagnostic X-ray energy range the refractive index of a material may be expressed as $n = 1 - \delta + i\beta$. The δ term is the real refractive index correction, which determines the refraction angle deviation that occurs at the interface between heterogeneous materials. The β term is the imaginary refractive index correction, which determines the amount of attenuation that occurs through a material. The real part of the refractive index correction is calculated by

$$\delta = \frac{r_e \lambda^2 \rho_e}{2\pi} = \frac{r_e \lambda^2}{2\pi u} \frac{Z}{A} \rho, \qquad (1)$$

where r_e is the classical electron radius ($r_e = 2.818 \times 10^{-15}$ m), λ is the X-ray wavelength, ρ_e is the electron density of the target material, u is the atomic mass unit, Z is the atomic number of the target material, A is the atomic mass of the target material, and ρ is the mass density of the target material (Als-Nielsen & McMorrow, 2001). For a composite object with n elements, (1) is used in a summation over all the components resulting in

$$\frac{\delta_{comp}}{\rho_{comp}} = \sum_{i=1}^{n} f_i \frac{\delta}{\rho_i}, \qquad (2)$$

where ρ_{comp} is the mass density of the composite object, δ_{comp} is the real part of the refractive index correction for the composite object, f_i is the mass fraction of the ith element, and δ/ρ_i is the real part of the refractive index correction for the ith element divided by the mass density of that element. The refraction angle deviation for a photon going from an initial media with refractive index n_1 to a second media with refractive index n_2 is given by Snell's law, $n_1 \sin\theta_1 = n_2 \sin\theta_2$, where θ_1 and θ_2 are the angles measured from their respective surface normal. Using Snell's law the deviation in angle for an X-ray passing through a material interface can be derived and is approximated by (Bewer, 2011)

$$\Delta\theta \cong (\delta_1 - \delta_2)\tan\theta_1 \simeq \frac{1}{4\pi}\frac{r_e\lambda^2}{u}(\rho_1 - \rho_2)\tan\theta_1, \quad (3)$$

where $\Delta\theta$ is the refraction angle deviation, $\delta_{1,2}$ is the real refractive index correction for the first and second material, respectively, $\rho_{1,2}$ is the mass density of the first and second target material, respectively, and θ_1 is the angle of incidence of the photon at the material interface measured from the surface normal. On the right-hand side of (3) the real refractive index correction terms have been replaced by mass density terms using (1).

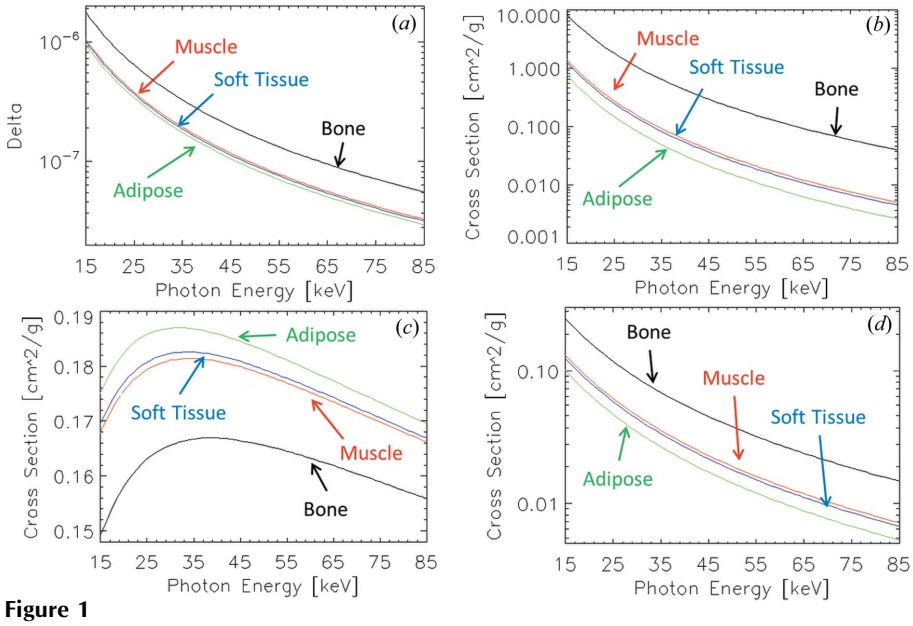

Figure 1
Physical properties for soft tissue, adipose tissue, skeletal muscle and compact bone. (*a*) Real refractive index corrections. (*b*) Photoelectric cross sections. (*c*) Incoherent scattering cross sections. (*d*) Coherent scattering cross sections.

1.2. Tissue compositions and cross sections

To determine the surface absorbed dose associated with either ABI or absorption-based imaging, where discerning the difference between biological tissues to a desired statistical certainty is the objective, a detailed understanding of the tissue composition is required. Lists of the elemental composition of soft tissue, adipose tissue, skeletal muscle and compact bone with fractions by weight are available from NIST.[1] The real refractive index correction may be calculated for these tissues using (1) and (2) and are plotted from 15 to 85 keV in Fig. 1(*a*).

The photoelectric absorption cross section, incoherent scattering cross section and coherent scattering cross sections were taken from NIST[2] and are plotted in Figs. 1(*b*)–1(*d*). The cross section in barns may be calculated from (Leo, 1994)

$$\frac{\mu}{\rho} = \frac{N_a}{A}\sigma, \quad (4)$$

where μ/ρ is the mass attenuation coefficient for the specific interaction, N_a is Avogadro's number, and σ is the interaction cross section in barns. The total mass attenuation coefficient is the sum of all three interactions and is denoted μ/ρ_T. The total linear attenuation coefficient is equal to the total mass attenuation coefficient multiplied by the mass density and is denoted μ_T. To be able to determine the surface absorbed dose delivered to a sample during X-ray imaging the absorbed energy mass attenuation coefficient is needed and is equal to the sum of the photoelectric absorption cross section and the absorption portion of the incoherent scattering cross section.

1.3. Darwin widths of crystal reflections

Each crystal reflection at a particular photon energy has a unique width of the double-crystal rocking curve. For the same crystal lattice the rocking curve becomes progressively narrower going to higher-order reflections, and for the same reflection higher-energy photons will have narrower rocking curves associated with them than lower photon energies. This means that the slope on the side of the rocking curve is greater in magnitude for higher-order reflections and larger photon energies and this smaller rocking-curve Darwin width corresponds to an increased sensitivity to X-ray angle deviations. For silicon crystals in the Bragg diffraction condition the Darwin width of four common reflections are plotted in Fig. 2 (James, 1962; Zachariasen, 1945).

The value of the Darwin width is calculated from

$$\omega_D = \frac{2hcr_e\, d_{hkl}|F_{hkl}|}{\pi E V_c \cos\theta_B}, \quad (5)$$

where h is Planck's constant, c is the speed of light in a vacuum, r_e is the classical electron radius, hkl are the Miller indices of the crystal reflection, d_{hkl} is the crystal lattice distance parameter for the hkl reflection, F_{hkl} is the structure

[1] Star database, National Institute of Standards and Technology, Gaithersburg, Maryland, USA; http://physics.NIST.gov/cgi-bin/Star/compos.pl?matno=001.
[2] XCOM database, National Institute of Standards and Technology, Gaithersburg, Maryland, USA; http://www.NIST.gov/pml/data/xcom/index.cfm.

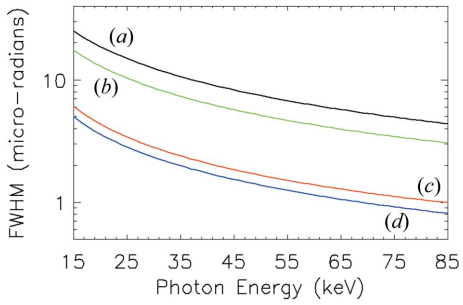

Figure 2
FWHM of the double-crystal rocking curve for common ABI silicon crystal reflections. (*a*) Si(1,1,1); (*b*) Si(2,2,0); (*c*) Si(4,4,0); (*d*) Si(3,3,3).

factor for the *hkl* reflection, E is the photon energy, V_c is the volume of the unit cell, and θ_B is the Bragg angle.

1.4. Detector properties

The area detectors considered in the following discussion are taken to be ideal with independent pixels that possess Poisson statistical characteristics and no inherent background noise. The detective quantum efficiency (DQE) is defined as α. For a given number of incident quanta over the surface area of the detector (N_0) the average number that interact will be $\overline{N} = \alpha\overline{N_0}$, where $\overline{N_0}$ is the mean value or expectation value of N_0. The gain of the detector is assumed to be unity so that the mean output signal of the detector, which is given by $\overline{d} = g\alpha\overline{N_0}$, equals the average number of quanta that interact (Cunningham, 2003; Zanella, 2002). For such an ideal detector with a beam of monochromatic X-rays incident on it the DQE of the detector will be approximated by the quantum efficiency of the detector given by

$$\alpha_{\rm det} = \frac{\mu^{\rm det}(E)/\rho_{\rm ea}}{\mu^{\rm det}(E)/\rho_{\rm T}}\left[1 - \exp\left(-\frac{\mu^{\rm det}(E)}{\rho_{\rm T}}\,\rho_{\rm det}\,t_{\rm det}\right)\right], \quad (6)$$

where $\mu^{\rm det}(E)/\rho_{\rm ea}$ is the energy absorption mass attenuation coefficient for the detector scintillation layer as a function of energy, $\mu^{\rm det}(E)/\rho_{\rm T}$ is the total mass attenuation coefficient for the detector scintillation layer as a function of energy, $\rho_{\rm det}$ is the mass density of the detector scintillation layer, and $t_{\rm det}$ is the projected thickness of the detector scintillation layer. As an example a detector with a 50 µm-thick layer of Gd_2O_2S is considered. The fraction of incident X-rays arriving at the detector which will contribute to the image is calculated using (6) and plotted in Fig. 3(*a*) from 15 to 85 keV. Hence the number of incident X-rays should be increased by the inverse of the DQE (Fig. 3*b*) to result in the expected number of X-rays contributing to the image. To obtain values for a particular system both the required imaging photon flux and the resulting surface absorbed dose calculated in the following section would need to be adjusted for the detector background noise, DQE and gain.

2. Method

To find the minimum surface absorbed dose to statistically distinguish between two different tissues with a 1σ certainty between pixels before image processing, where one pixel has an embedded object in the path and the other does not, an understanding of the geometry of the sample is required. The case that will be considered is a 1 mm-thick piece of adipose tissue, soft tissue or bone embedded in the middle of a 5 cm piece of soft tissue or adipose tissue. These tissue thicknesses are chosen to correspond to common working distances for research using animal models utilizing rats and small animals. For ABI imaging an average angle of incidence at the boundary interface between the two sample materials is assumed to be 45° so that $\tan\theta = 1$. All other angles may then be determined from this case by multiplying by the appropriate angle factor. For conventional absorption-based imaging no propagation phase contrast is assumed and the angle of incidence at the boundary is not important, only the total path lengths through the materials (Fig. 4). Poisson statistical errors are used throughout the analysis so that the square root of the photon count in each pixel is the standard deviation.

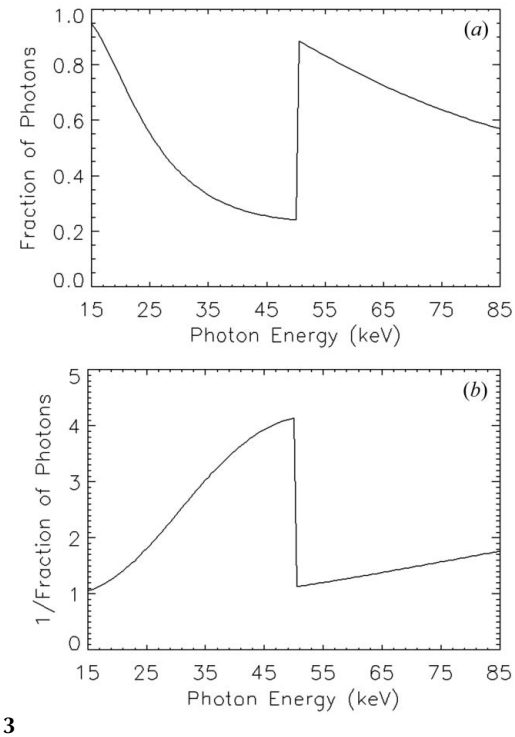

Figure 3
(*a*) The fraction of X-rays incident on the detector resulting in absorbed energy for a 50 mm-thick layer of Gd_2O_2S as a function of photon energy. This is an approximation of the ideal detector's DQE. (*b*) Inverse of (*a*) and the DQE correction factor when determining the required number of incident X-rays.

2.1. Absorption imaging

For the sample geometry shown in Fig. 4 the equation giving the minimum incident number of photons on the sample per pixel area allowing the embedded tissue to be resolved with a 1σ statistical certainty using absorption imaging at the thickest part is given by solving (7). If the embedded material has less stopping power than the surrounding material then the sign of

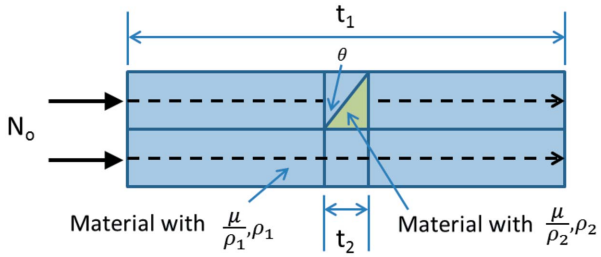

Figure 4
Geometric configuration of a theoretical sample. For ABI the angle with respect to the incident photon at the density change is important, whereas only the total path lengths through the materials are important for absorption imaging.

the last term in (7) is positive. If the embedded material has more stopping power than the surrounding material then the sign of the last term in (7) is negative,

$$N_0^{\rm abs}\exp\left[-\frac{\mu}{\rho_1}\rho_1(t_1-t_2)\right]\exp\left(\frac{-\mu}{\rho_2}\rho_2 t_2\right) = N_0^{\rm abs}\exp\left(\frac{-\mu}{\rho_1}\rho_1 t_1\right) \pm \left[N_0^{\rm abs}\exp\left(\frac{-\mu}{\rho_1}\rho_1 t_1\right)\right]^{1/2}, \quad (7)$$

where $\mu/\rho_{1,2}$ is the total mass attenuation coefficient for the first and second material, respectively, $\rho_{1,2}$ is the mass density of the first and second material, respectively, $t_{1,2}$ is the thickness of the first and second material, respectively, and $N_0^{\rm abs}$ is the minimum incident number of photons on the sample that allows the embedded tissue to be resolved with a 1σ statistical certainty using absorption imaging. Using a monochromatic beam the value of $N_0^{\rm abs}$ would equal the fluence or photon fluence from which energy fluence and other radiographic quantities can be calculated (Johns & Cunningham, 1983).

Regardless of which sign is chosen in (7) the resulting number of required photons per pixel is the same and is given by (8). The value of $N_0^{\rm abs}$ calculated by (8) will always be multiplied by a factor of five in the following discussion to account for the use of a crossed anti-scatter grid with a ratio of 8, which is common for high-contrast absorption radiographic images (Hendee & Ritenour, 2002). These grids, when used in contact between the sample and imaging plate, allow only X-rays that have been deviated by 7.2° or less to pass through,

$$N_0^{\rm abs} = \exp\left[-(\mu/\rho_1)\rho_1 t_1\right] \Big/ \Big\{ \exp\left[-(\mu/\rho_1)\rho_1(t_1-t_2)\right]^2 \exp\left[-(\mu/\rho_2)\rho_2 t_2\right]^2 - 2\exp\left[-(\mu/\rho_1)\rho_1(t_1-t_2)\right]\exp\left[-(\mu/\rho_2)\rho_2 t_2\right] \times \exp\left[-(\mu/\rho_1)\rho_1 t_1\right] + \exp\left[-(\mu/\rho_1)\rho_1 t_1\right]^2 \Big\}. \quad (8)$$

2.2. Analyzer-based imaging

The equation giving the minimum number of incident photons on the sample per pixel area allowing the embedded tissue to be resolved with a 1σ statistical certainty for the sample shown in Fig. 4 at the thickest part using ABI is given by (9) (see Appendices *A* and *B*),

$$N_0^{\rm DEI} = \left\{R(\theta_{1/2})/[({\rm d}R/{\rm d}\theta)\Delta\theta]\right\}^2 \times \frac{1}{\exp\left\{-\left[(\mu/\rho_1)\rho_1(t_1-t_2)+(\mu/\rho_2)\rho_2 t_2\right]\right\}}\frac{1}{R(\theta_{1/2})}. \quad (9)$$

For ABI, when the linear side regions of the rocking curve are used, the value of ${\rm d}R/{\rm d}\theta$ may be approximated as $1/\omega_{\rm D} \cong 1/{\rm FWHM}$ for the various crystal reflections (Fig. 2). ABI measurements using points on the rocking curve other than the half-intensity positions would require the crystal reflectivity values used in (9) to be changed to the new position, $R(\theta_{1/2}) \rightarrow R(\theta_f)$. Lastly, the average angle of incidence of 45° assumed earlier results in $\Delta\theta = \Delta\delta = (1/4\pi)(r_e\lambda^2/u)\Delta\rho$ as indicated by (3).

2.3. Calculation of the number of required photons

Using (8) and (9) the number of incident photons on the sample required per pixel area to obtain a raw image with a 1σ statistical variation between tissues was found for bone embedded in soft tissue, bone embedded in adipose tissue, adipose tissue embedded in soft tissue, and soft tissue embedded in adipose tissue [Figs. 5(*a*)–5(*d*)]. The thickness of the embedded material was taken to be 1 mm and the surrounding tissue was taken to be 5 cm. The embedded tissue was assumed to be in the middle of the surrounding tissue.

Fig. 5 indicates that using a low-order silicon crystal reflection with the ABI technique will not result in a significantly lower number of required incident X-rays compared with absorption-based imaging using a crossed anti-scatter grid with a ratio of 8. However, the difference in incident photons required between the two lower silicon reflections and the two higher-order reflections is approximately an order of magnitude for the entire 15–85 keV energy range and shows the benefit of a narrower rocking curve with additional sensitivity to angle deviations.

It can be seen in Fig. 5 that the minimum number of photons required takes place towards the lower imaging energies. This may seem counter-intuitive as less absorption would occur in the sample at higher energies and the Darwin width of each crystal reflection progressively decreases towards higher photon energies giving more sensitivity to refraction angle deviations in the sample. However, the gains from less sample absorption and a narrower rocking curve is offset by the real refractive index correction for each material becoming smaller at higher energies which is proportional to $1/E^2$ as shown in (3). The change in the crystal reflection Darwin width by comparison is proportional to $1/E$ as shown in (5), and Fig. 1 indicates that after 25 keV the dominant photon interaction is incoherent scattering which is approximately proportional to $1/E$. Therefore any further reductions in photoelectric absorption at higher energies will not reduce the required number of incident photons for imaging.

The values in Fig. 5 are for an ideal detector and would be modified for a true system by the background noise, DQE and gain values of the detector used during measurements. A change between different detectors will alter the value of the ideal imaging energy for that system.

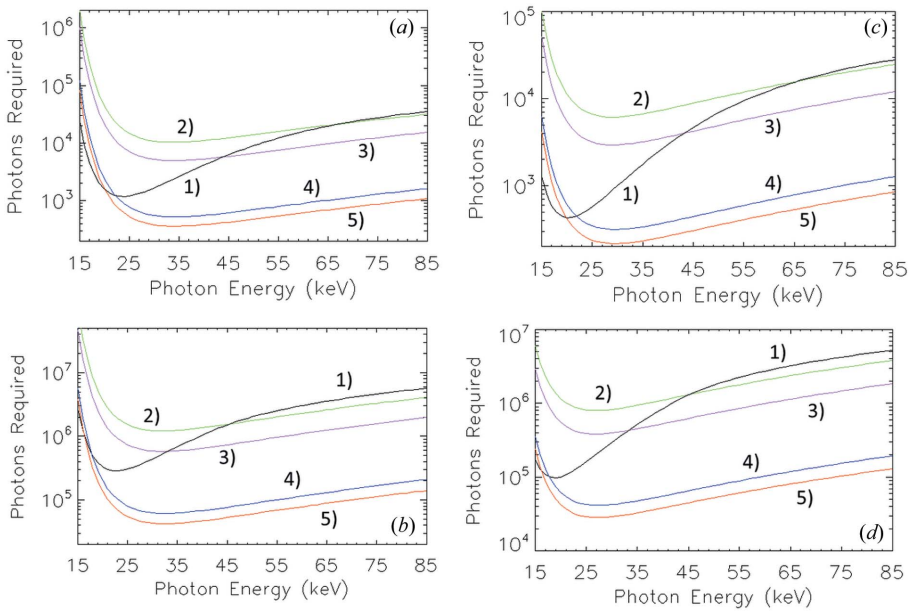

Figure 5
Number of incident photons on the sample required per pixel area to distinguish between the embedded object and the surrounding material with a 1σ statistical certainty. The presented values are for an ideal detector with zero background noise and unity DQE and gain at all energies. (*a*) 1 mm of bone embedded in 5 cm of soft tissue. (*b*) 1 mm of adipose tissue embedded in 5 cm of soft tissue. (*c*) 1 mm of bone embedded in 5 cm of adipose tissue. (*d*) 1 mm of soft tissue embedded in 5 cm of adipose tissue. (1) Absorption-based imaging using a crossed anti-scatter grid and no propagation phase-contrast enhancement; (2) ABI using Si(1,1,1); (3) ABI using Si(2,2,0); (4) ABI using Si(4,4,0); (5) ABI using Si(3,3,3).

2.4. Dose calculations

The X-ray imaging surface absorbed dose in kGy is calculated using

$$D_s = \frac{N_0 E_{ph}}{A} \frac{\mu(E_{ph})}{\rho_{ea}} \rho, \qquad (10)$$

where N_0 is the incident photon count calculated from (8) or (9), E_{ph} is the energy of the incident photons in Joules, and A is the area and is defined by the detector pixel size in this discussion.

When the embedded material is similar in density to the surrounding material the entrance dose will be the highest-dosed surface. When a dense material is embedded in a lighter material the entrance dose may not necessarily be the most highly dosed surface. In these cases the entrance dose and the surface between the lighter material and denser embedded material should both be examined to determine which receives the highest dose.

Using the number of incident photons on the sample per pixel area plotted in Fig. 5, the absorbed energy mass attenuation coefficient as a function of energy, the mass density for soft tissue and a detector pixel size of 20 µm, the resulting surface absorbed dose values in mGy are shown in Fig. 6. The dose values given in Fig. 6 are for a single image using the number of photons calculated from (9) for absorption imaging and double the number of photons given in (10). This doubling is because the ABI method requires two images, one at each of the half-intensity points on the rocking curve, to solve for absorption and refraction images. For 1 mm of compact bone embedded in the middle of 5 cm of soft tissue the bone surface is the highest-dosed surface above an imaging energy of 18.5 keV. For 1 mm of bone embedded in the middle of 5 cm of adipose tissue the bone surface is the highest-dosed surface over the entire image energy range considered. For the two other cases the entrance surface is always the highest-dosed surface.

Fig. 6 indicates that for bone embedded in soft tissues there are only small differences in the delivered maximum surface absorbed dose in the 40–80 keV photon energy range. However, when only soft tissues are involved there is a clear minimum that occurs in the 35–50 keV photon energy range. Thus the Gd_2O_2S detector discussed in §1.4 would be suitable

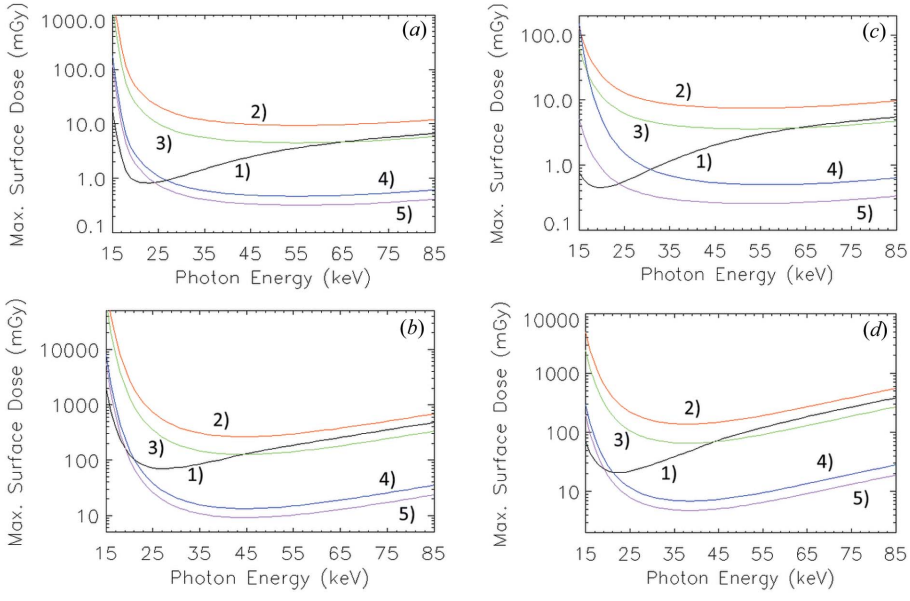

Figure 6
Maximum surface absorbed dose resulting from imaging using the incident photon flux numbers from Fig. 5. (*a*) 1 mm of bone embedded in 5 cm of soft tissue. (*b*) 1 mm of adipose tissue embedded in 5 cm of soft tissue. (*c*) 1 mm of bone embedded in 5 cm of adipose tissue. (*d*) 1 mm of soft tissue embedded in 5 cm of adipose tissue. Imaging method: (1) absorption imaging using a crossed anti-scatter grid and no propagation phase-contrast enhancement; (2) ABI using Si(1,1,1); (3) ABI using Si(2,2,0); (4) ABI using Si(4,4,0); (5) ABI using Si(3,3,3).

for bone imaging around 50 keV, and would perform reasonably well for soft tissue imaging at the same energy for the example sizes considered.

3. Discussion and conclusions

In the previous sections the analysis determined the number of incident photons on the sample required per pixel area for a 1σ statistical difference in the raw image between a pixel with the embedded object in the path and a pixel with only the bulk material in the path. The associated surface absorbed dose value for both conventional absorption-based imaging and ABI imaging where the average angle of incidence of the photons on the surface boundary is 45° was determined. It should be noted that both the apparent absorption image and the refraction angle image from the ABI method require either the sum or the difference of the two raw images, each of which has 1σ statistical variation between tissues. This post-image processing of the raw data would result in an image which has less than the original statistical significance by a factor of $1/\sqrt{2}$ between the embedded tissue and the surrounding soft tissue. However, all ABI images benefit from microradian-level scatter rejection compared with 7.2° in absorption imaging using a crossed grid with ratio of 8. To find the number of incident photons needed for 2σ statistical certainties we need only solve equations (7) and (18) for twice the Poisson standard deviation. Bringing this factor of two inside the square-root term reveals that for 2σ statistical certainty four times the 1σ value is required. In general, if an $n\sigma$ statistical certainty is desired between pixels with the embedded object in the path and those without them, n^2N_1 X-rays are needed, where N_1 is the 1σ incident number of X-rays. The surface absorbed dose will also change by the same n^2 factor whenever the incident number of X-rays changes by n^2.

For ABI a change of the refraction angle deviation term by integer multiples has an n^2 effect on the required number of incident photons. Depending on the geometry of the sample it may be valid to assume a different value for the average angle of incidence at the material boundary in the ABI analysis. As Kiss *et al.* (2003) demonstrated, if the object of interest is cylindrical and the curvature of the cylinder is in the diffraction plane, then the net refraction angle deviation through the cylindrical object would be doubled. This doubling of the average θ value, either by changing θ from 45° to 63.4° or by two refractions at 45°, results in twice the refraction angle deviation,

$$\Delta\theta = \Delta\delta \tan 63.4^\circ = 2\Delta\delta \tan 45^\circ. \quad (11)$$

The number of photons required per pixel to achieve the original level of statistical certainty with this new refraction angle deviation would then be four times less than before. If the same number of photons per pixel is used anyway, then the resulting image would have double the statistical certainty between pixels with the embedded object in the path and those without. One of the consequences of relying on larger refraction angle deviations to achieve the desired statistical variations between pixels is that the detector pixel size required to resolve these differences becomes smaller. Using Fig. 7 as an example, the region on the object where the angle of incidence measured from the surface normal (θ) is greater than the chosen average value results in a vertical projected size that is calculable by

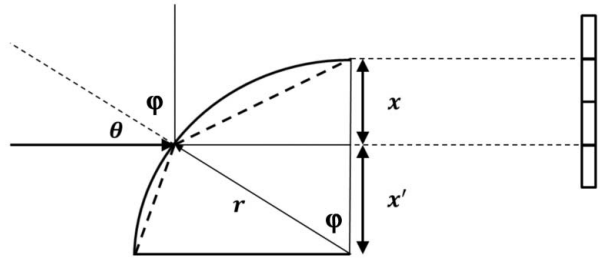

Figure 7
The vertical size of the region where the angles of incidence are greater than the desired average angle is given by x.

$$x(\varphi) = r - x' = r - r\cos(\varphi) = r[1 - \cos(90^\circ - \theta)]. \quad (12)$$

This vertical size will determine the maximum allowable detector pixel dimension that can be used and still achieve the desired statistical variations between materials at the calculated dose level. Since detector pixel alignment over the desired feature cannot be assured, the size calculation in (12) is a limit. Smaller pixel sizes would be preferable assuming the resulting additional dose is not prohibitive. Using a detector pixel larger than calculated in (12) could result in a portion of the pixel being located in a region with lower than desired X-ray signal. The final value would then be the average of the region containing the desired signal level (or more) with the low signal region and may result in a smaller statistical variation between materials than intended. It should also be noted that for an object with varying thickness the maximum thickness (or the most highly absorbing region) should be chosen when calculating the necessary number of incident photons on the sample per pixel area so that the thickest or most dense region has the desired certainty and all other regions of the object that are less thick or less absorbing have better than desired statistical differences.

The presented work featured only two materials in the object, but the absorption and ABI calculations can be generalized for a composite sample of many materials. For ABI samples with n materials, each with a well defined real refractive index correction, mass attenuation coefficient, density, thickness and $n-1$ boundaries between those materials, (16) and (17) in Appendix A generalize to

$$N_{\mathrm{L,H}} = N_0 \prod_{i=1}^{n} \exp\left(-\frac{\mu}{\rho_i}\rho_i t_i\right) \times \left[R\left(\theta_{\mp f}\right) \pm \sum_{i=1}^{n-1} \frac{\mathrm{d}R}{\mathrm{d}\theta} \Delta\delta_{i,i+1} \tan\theta_{i,i+1}\right], \quad (13).$$

where $N_{\mathrm{L,H}}$ are the measurements on the low-angle and high-angle side of the rocking curve, respectively, N_0 is the number of incident photons on the sample per pixel area, n is the number of materials, μ/ρ_i is the mass attenuation coefficient

for the ith material, ρ_i is the mass density of the ith material, t_i is the thickness of the ith material, $R(\theta_{\mp f})$ are the crystal reflectivity values on the low-angle and high-angle side of the rocking curve where the measurements are taken, $\mathrm{d}R/\mathrm{d}\theta$ is the slope of the rocking curve at the location of a measurement, $\Delta\delta_{i,i+1}$ is the real refractive index difference between the ith and $(i+1)$th materials, and $\theta_{i,i+1}$ is the angle of incidence of the X-ray on the boundary between the ith and $(i+1)$th materials. In such an object, caution when predicting the number of incident photons required would be needed as the possibility of several overlapping embedded objects, some perhaps with higher density variations than the one of interest, are possible and will alter the ability to distinguish the desired feature.

APPENDIX *A*
ABI equations

For ABI the measurement locations are the high- and low-angle half-maximum intensity points on the rocking curve (N_H, N_L). This allows the assumptions $R(\theta) = R(\theta_{1/2}) + (\mathrm{d}R/\mathrm{d}\theta)\Delta\theta$, $R(\theta_{1/2}) = 1/2$ and $\mathrm{d}R/\mathrm{d}\theta = 1/\omega_\mathrm{D}$ to be made, where $R(\theta)$ is the reflectivity of the crystal at the imaging photon energy for the angle θ, $\theta_{1/2}$ is the incident angle at which the crystal reflectivity is equal to half of the maximum, $\mathrm{d}R/\mathrm{d}\theta$ is the slope of the crystal reflectivity at the location of the measurement, and ω_D is the Darwin width of the crystal reflection. The photon count measured through the ABI system at an angle θ with the geometry from Fig. 4 with the above assumptions is given by

$$N_\theta = N_0 \exp\left\{-\left[\frac{\mu}{\rho_1}\rho_1(t_1 - t_2) + \frac{\mu}{\rho_2}\rho_2 t_2\right]\right\} R(\theta). \tag{14}$$

Substituting for the variable $R(\theta)$ results in

$$N_\theta = N_0 \exp\left\{-\left[\frac{\mu}{\rho_1}\rho_1(t_1 - t_2) + \frac{\mu}{\rho_2}\rho_2 t_2\right]\right\} \times \left[R(\theta_{1/2}) \pm \frac{\mathrm{d}R}{\mathrm{d}\theta}\Delta\theta\right]. \tag{15}$$

The two equations for the low-angle side of the rocking curve and the high-angle side are thus given by taking the positive and negative sign in (15), respectively.

When the two cases of (15) are summed together, the angle deviation terms cancel and the result is a formula to form the apparent absorption image (apparent because scatter extinction is indistinguishable from absorption in ABI) given by

$$\begin{aligned} N_\mathrm{L} + N_\mathrm{H} &= 2N_0 \exp\left\{-\left[\frac{\mu}{\rho_1}\rho_1(t_1 - t_2) + \frac{\mu}{\rho_2}\rho_2 t_2\right]\right\} R(\theta_{1/2}) \\ &= 2N_0 \exp\left\{-\left[\frac{\mu}{\rho_1}\rho_1(t_1 - t_2) + \frac{\mu}{\rho_2}\rho_2 t_2\right]\right\} \left(\frac{1}{2}\right) \\ &= N_0 \exp\left\{-\left[\frac{\mu}{\rho_1}\rho_1(t_1 - t_2) + \frac{\mu}{\rho_2}\rho_2 t_2\right]\right\}. \end{aligned} \tag{16}$$

To arrive at the formula for the refraction angle image the difference of the low- and high-angle measurements is divided by the sum of the two measurements and is given by (17) where substitutions from the list of assumptions have been used,

$$\begin{aligned} \frac{N_\mathrm{L} - N_\mathrm{H}}{N_\mathrm{L} + N_\mathrm{H}} &= \frac{(\mathrm{d}R/\mathrm{d}\theta)\Delta\theta}{R(\theta_{1/2})} \\ \rightarrow \Delta\theta &= \frac{R(\theta_{1/2})}{\mathrm{d}R/\mathrm{d}\theta}\frac{N_\mathrm{L} - N_\mathrm{H}}{N_\mathrm{L} + N_\mathrm{H}} = \frac{\omega_\mathrm{D}}{2}\frac{N_\mathrm{L} - N_\mathrm{H}}{N_\mathrm{L} + N_\mathrm{H}}. \end{aligned} \tag{17}$$

APPENDIX *B*
Minimum number of photons to distinguish between materials using ABI

To find the minimum number of photons necessary to distinguish an embedded tissue from the surrounding soft tissue with a 1σ statistical certainty in the pixel count using the ABI method, we start with the condition that the refracted beam photon count is equal to the non-refracted beam photon count plus the square-root of the non-refracted beam photon count,

$$N_\theta|_{\theta=\theta_{1/2}+\Delta\theta} = N_\theta|_{\theta=\theta_{1/2}} + \left(N_\theta|_{\theta=\theta_{1/2}}\right)^{1/2}. \tag{18}$$

Substituting (15) for the first term in (18) and rearranging results in

$$\begin{aligned} N_\theta|_{\theta=\theta_{1/2}} + N_\theta|_{\theta=\theta_{1/2}}\frac{\mathrm{d}R}{\mathrm{d}\theta}\frac{\Delta\theta}{R(\theta_{1/2})} &= N_\theta|_{\theta=\theta_{1/2}} + \left(N_\theta|_{\theta=\theta_{1/2}}\right)^{1/2} \\ \rightarrow N_\theta|_{\theta=\theta_{1/2}} &= \left[\frac{R(\theta_{1/2})}{(\mathrm{d}R/\mathrm{d}\theta)\Delta\theta}\right]^2. \end{aligned} \tag{19}$$

Replacing the left side of (19) with (15) and solving for N gives the equation for the number of incident photons on the sample needed to resolve the embedded material from the detector pixel count with a 1σ statistical certainty (before detector efficiency corrections) and is given by

$$\begin{aligned} N_0 \exp\left\{-\left[\frac{\mu}{\rho_1}\rho_1(t_1 - t_2) + \frac{\mu}{\rho_2}\rho_2 t_2\right]\right\} R(\theta_{1/2}) &= \left[\frac{R(\theta_{1/2})}{(\mathrm{d}R/\mathrm{d}\theta)\Delta\theta}\right]^2 \\ \rightarrow N_0^\mathrm{DEI} = \left[\frac{R(\theta_{1/2})}{(\mathrm{d}R/\mathrm{d}\theta)\Delta\theta}\right]^2 &\frac{1}{\exp\left\{-\left[\frac{\mu}{\rho_1}\rho_1(t_1 - t_2) + \frac{\mu}{\rho_2}\rho_2 t_2\right]\right\}} \\ &\times \frac{1}{R(\theta_{1/2})}. \end{aligned} \tag{20}$$

Brian Bewer is an Associate Member of the Canadian Institutes of Health Research Training program in Health Research Using Synchrotron Techniques (CIHR-THRUST). The research described in this paper was performed at the Canadian Light Source, which is supported by the Natural Sciences and Engineering Research Council of Canada, the National Research Council Canada, the Canadian Institutes of Health Research, the Province of Saskatchewan, Western Economic Diversification Canada, and the University of Saskatchewan.

References

Als-Nielsen, J. & McMorrow, D. (2001). *Elements of Modern X-ray Physics*. New York: John Wiley and Sons.

Bewer, B. (2011). *Nucl. Instrum. Methods Phys. Res. A*, **646**, 197–199.

Chapman, D., Thomlinson, W., Johnston, R. E., Washburn, D., Pisano, E., Gmur, N., Zhong, Z., Menk, R., Arfelli, F. & Sayers, D. (1997). *Phys. Med. Biol.* **42**, 2015–2025.

Cooper, D. M. L., Bewer, B., Wiebe, S., Belev, G., Wysokinski, T. & Chapman, L. D. (2011*a*). *Synchrotron Radiat. News*, **24**, 13–18.

Cooper, D. M. L., Bewer, B., Wiebe, S., Wysokinski, T. W. & Chapman, D. (2011*b*). *Can. Assoc. Radiol. J.* **62**, 251–255.

Cunningham, I. A. (2003). *Advanced Imaging Principles: Course Notes*. Department of Medical Biophysics, University of Western Ontario, Canada.

Hendee, W. R. & Ritenour, E. R. (2002). *Medical Imaging Physics*, 4th ed. New York: Wiley-Liss.

James, R. W. (1962). *The Optical Principles of the Diffraction of X-rays*. Woodbridge: Ox Bow Press.

Johns, H. E. & Cunningham, J. R. (1983). *The Physics of Radiology*, 4th ed. Springfield: Charles C. Thomas.

Keyriläinen, J., Fernández, M., Fiedler, S., Bravin, A., Karjalainen-Lindsberg, M.-L., Virkkunen, P., Elo, E.-M., Tenhunen, M., Suortti, P. & Thomlinson, W. (2005). *Eur. J. Radiol.* **53**, 226–237.

Kiss, M. Z., Sayers, D. E. & Zhong, Z. (2003). *Phys. Med. Biol.* **48**, 325–340.

Leo, W. R. (1994). *Techniques for Nuclear and Particle Physics Experiments*, 2nd ed. New York: Springer-Verlag.

Pisano, E. D., Johnston, R. E., Chapman, D., Geradts, J., Iacocca, M. V., Livasy, C. A., Washburn, D. B., Sayers, D. E., Zhong, Z., Kiss, M. Z. & Thomlinson, W. C. (2000). *Radiology*, **214**, 895–901.

Rigon, L., Arfelli, F. & Menk, R.-H. (2007). *Appl. Phys. Lett.* **90**, 114102.

Zachariasen, W. H. (1945). *Theory of X-ray Diffraction in Crystals*. New York: Wiley.

Zanella, G. (2002). *Nucl. Instrum. Methods Phys. Res. A*, **481**, 691–695.